

# Three-dimensional near-field microwave imaging with multiple-input multiple-output coded generalized reduced dimension Fourier algorithm

Amir Masoud Molaei<sup>\*a</sup>, Shaoqing Hu<sup>b</sup>, Rupesh Kumar<sup>c</sup>, Okan Yurduseven<sup>a</sup>

<sup>a</sup>Centre for Wireless Innovation (CWI), Queen's University Belfast, Queen's Road, Belfast, U.K. BT3 9DT; <sup>b</sup>College of Engineering, Design and Physical Sciences, Brunel University London, Kingston Lane, Uxbridge, U.K. UB8 3PH; <sup>c</sup>Department of Electronics and Communication Engineering, SRM University-AP, Andhra Pradesh, India 522502

## ABSTRACT

This paper introduces an approach for 3-D near-field microwave imaging, combining a special 2-D multiple-input multiple-output (MIMO) structure with orthogonal coding and Fourier domain processing. The proposed MIMO coded generalized reduced dimension Fourier algorithm effectively reduces data dimensionality while preserving valuable information, streamlining image reconstruction. Through mathematical derivations, we show how the proposed approach includes phase and amplitude compensators and reduces the computational complexity. The algorithm includes both phase and amplitude compensators, reduces the computational complexity, and mitigates propagation loss effects. Numerical simulations confirm the approach's satisfactory performance in terms of information retrieval and processing speed.

**Keywords:** Coded generalized reduced dimension Fourier algorithm, MIMO, near-field, 3-D microwave imaging

## 1. INTRODUCTION

Near-field (NF) microwave radar imaging has become indispensable in various fields such as medical diagnosis, security screening and structural health monitoring [1-6]. However, the challenge of synthesizing a 2-D aperture for 3-D imaging often demands many antenna elements to satisfy the Nyquist criterion [7]. Using sparse aperiodic phased arrays and (multiple-input multiple-output) MIMO arrays can reduce complexity and enhance image quality [8-11]. MIMO arrays offer the advantage of simultaneous transmission and reception, which reduces data acquisition time. Orthogonal coding is used to effectively distinguish between transmitter-receiver (TX-RX) channels, though existing methods may be complex [12, 13].

To address the above challenges, namely the need for large antenna arrays, the high computational demands of current methods and the complexity of managing simultaneous transmissions in MIMO systems, in this paper, we propose an approach utilizing a special 2-D MIMO structure to electronically synthesize the aperture, addressing the issue of data acquisition time and complexity. Our approach integrates orthogonal coding with Fourier domain processing, presenting a MIMO coded generalized reduced dimension Fourier algorithm. This algorithm effectively reduces the dimensionality of raw spatial data from 4-D to 2-D, streamlining image reconstruction while preserving valuable information. We introduce an efficient model for transmission and reception, leveraging orthogonal coded signals to enable simultaneous transmission by all TXs and separate extraction of channel information. Through mathematical derivations, we show how the proposed approach includes phase and amplitude compensators and reduces the computational complexity. Moreover, it mitigates common propagation loss effects in reconstructed images. Numerical simulations validate the proposed approach, demonstrating its satisfactory performance in terms of information retrieval and processing speed. Key contributions include introducing a 2-D MIMO structure for aperture synthesis, employing orthogonal code sequences to access multiple channels, and deriving an efficient algorithm for image reconstruction in NF microwave imaging.

<sup>\*</sup>a.molaei@qub.ac.uk; fax 44 28 9097 1702; pure.qub.ac.uk/en/persons/amir-masoud-molaei

The rest of this paper is organized as follows. Section 2 covers the system and data model. Section 3 deals with the presentation of the transfer function extraction procedure. In Section 4, the details of the image reconstruction are presented. Section 5 presents and discusses the simulation results. Finally, Section 6 offers the conclusion.

*Notation:* Throughout the paper, the symbols  $j$ ,  $\mathbf{I}_m$ ,  $\mathbf{0}_m$ ,  $\mathbf{1}_m$ ,  $\mathbf{A}(a:b, c:d)$ ,  $\hat{x}$ ,  $(\cdot)^T$  and  $\mathbb{E}\{\cdot\}$  denote the imaginary unit,  $m \times m$  identity and zero matrices,  $m \times 1$  vector with all entries equal to one,  $a$ -th to  $b$ -th rows and  $c$ -th to  $d$ -th columns of matrix  $\mathbf{A}$ , an estimate of  $x$ , transpose, and expected value operator, respectively.

## 2. SYSTEM AND DATA MODEL

In the proposed approach, radar measurements are obtained entirely electronically using two uniform rectangular arrays (URAs) as the TX and RX in a multistatic MIMO configuration (see Figure 1). The TX and RX URAs consist of  $N_x \times N_y$  and  $N'_x \times N'_y$  antenna elements, respectively, with inter-element spacings of  $d_x$  and  $d'_x$  along the horizontal and  $d_y$  and  $d'_y$  along the vertical. To create a uniform effective aperture with evenly spaced virtual elements, there must be a specific relationship between the number of antennas and their spacing. This uniform synthesized aperture is crucial for the development of the algorithm introduced in Section 3, which relies on fast Fourier calculations. According to the effective phase center principle, under the far-field (FF) assumption, if  $d_x = N'_x d'_x$  and  $d_y = N'_y d'_y$  are chosen, the resulting effective aperture will be a monostatic virtual URA with dimensions  $N \times N'$  and inter-element spacings of  $d = d'_x/2$  and  $d' = d'_y/2$ , where  $N = N_x \times N'_x$  and  $N' = N_y \times N'_y$  [13, 14]. Later in Section 3, we will show how to adapt such a structure for use in the NF scenario.

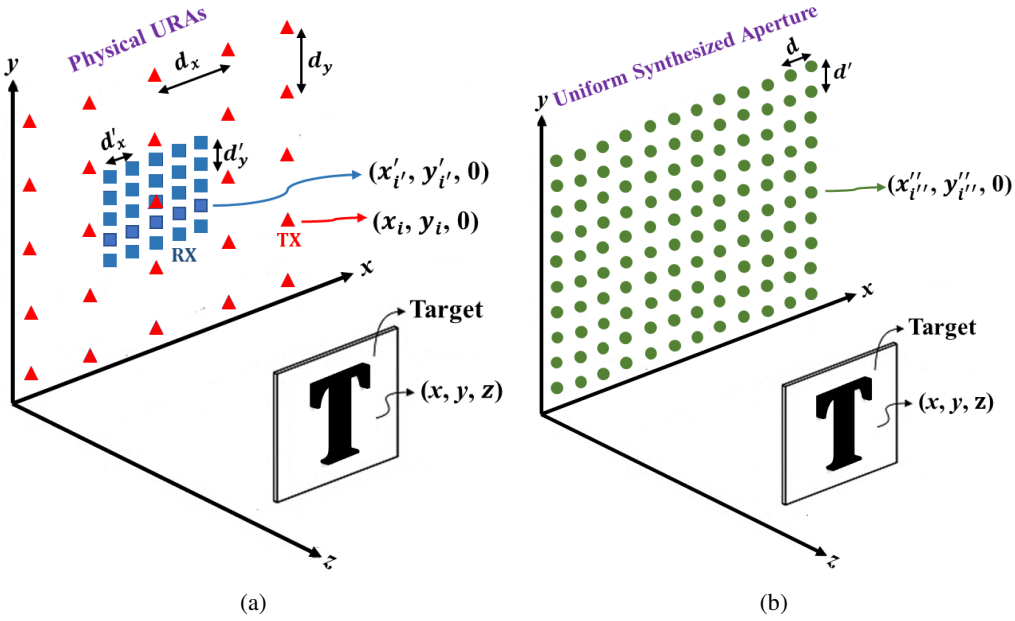


Figure 1. The overall configuration of the MIMO TX-RX arrays in the proposed approach; (a) multistatic physical arrays, (b) an equivalent monostatic virtual array assuming the FF condition.

To illuminate the scene, a stepped-frequency-modulated MIMO radar is used. Each TX antenna emits a binary phase-shift keying modulated signal based on a column of the matrix of binary code symbols (i.e.  $\Phi_{L \times N_T} \triangleq [\varphi_1, \varphi_2, \dots, \varphi_{N_T}]$ ) that meet the mutual orthogonality condition [13], where  $L$  is the code length,  $N_T = N_x \times N_y$ ,  $\varphi_i \triangleq [\varphi_{1,i}, \varphi_{2,i}, \dots, \varphi_{L,i}]^T$ ,  $\varphi_{l,i} \in \{-1, +1\}$ ,  $l = 1, 2, \dots, L$  and  $i = 1, 2, \dots, N_T$ . The received signal by the  $i'$ -th RX antenna can be modeled as a sum of the backscatter responses from all the TX antennas, affected by measurement noise  $n_{i'}[l]$ . The backscatter frequency

response  $H_{i,i'}$  depends on the reflectivity and propagation delay of hypothesized point scatterers in the scene [13]. After down-conversion and sampling, the received signal can be expressed in the following form [13]:

$$s_{i'}[l] = \sum_{i=1}^{N_T} H_{i,i'}(f) \phi_{i,i} + n_{i'}[l], \quad i' = 1, 2, \dots, N_R, \quad (1)$$

where  $f$  is the carrier frequency and  $N_R = N'_x \times N'_y$ .

### 3. TRANSFER FUNCTION EXTRACTION

A Hadamard matrix  $\mathbf{W}_{L \times L}$  [15] of order  $L$  is a square matrix with elements of  $\pm 1$ , where  $L$  can be 1, 2, or a multiple of 4. The matrix has orthogonal columns (or rows), meaning each vector is distinct and orthogonal to the others. Therefore, Hadamard matrices satisfy the orthogonality condition. When selecting code sequences, it is also crucial that they are balanced, meaning the number of  $-1$  and  $+1$  bits is equal. This balance ensures efficient decoding by processors [16]. Fortunately, the columns of a Hadamard matrix (except the first column) are inherently balanced. Therefore, we can simply exclude the first column, and the remaining columns will maintain orthogonality and balance. Hence, in this paper, we consider the matrix of binary code symbols as  $\mathbf{\Phi} = \mathbf{W}(1:L, 2:N_T + 1)$ , where  $\mathbf{\Phi}^T \mathbf{\Phi} = L \mathbf{I}_{N_T}$  and  $\mathbf{\Phi}^T \mathbf{1}_L = \mathbf{0}_{N_T}$ .

According to the above and (1), and by collecting and concatenating  $L$  samples received by the  $i'$ -th RX at frequency  $f$ , the received signal can be expressed in matrix form as:

$$\mathbf{s}_{i'} = \mathbf{\Phi} \mathbf{H}_{i'}(f) + \mathbf{n}_{i'}. \quad (2)$$

Due to the orthogonality property in the matrix  $\mathbf{\Phi}$ , the channel transfer function can be estimated as:

$$\hat{\mathbf{H}}_{i'}(f) = \frac{1}{L} \mathbf{\Phi}^T \mathbf{s}_{i'}. \quad (3)$$

### 4. IMAGE RECONSTRUCTION

The 3-D reconstruction of a scene's image involves estimating the spatial reflectivity function  $\rho(x, y, z)$  [17], which impacts the backscatter frequency response (also known as the channel transfer function) as described in Section 3. Based on the system's geometry shown in Figure 1(a), this backscatter frequency response can be expressed as a spatial-frequency relationship as [13, 18-20]

$$H(x_i, x'_i, y_i, y'_i, f) = \int_V \frac{\rho(x, y, z)}{16\pi^2 R_i R'_i} e^{-jk(R_i + R'_i)} dV, \quad (4)$$

where  $k = 2\pi f/c$  is the wavenumber,  $c$  is the speed of light, and  $dV = dx dy dz$  denotes a small volume element made of space intervals  $dx$ ,  $dy$  and  $dz$  in the directions  $x$ ,  $y$  and  $z$ , respectively. The distances  $R_i$  and  $R'_i$  are given by

$$R_i = \sqrt{(x - x_i)^2 + (y - y_i)^2 + z^2}, \quad (5)$$

$$R'_i = \sqrt{(x - x'_i)^2 + (y - y'_i)^2 + z^2}. \quad (6)$$

Since the backscatter frequency response is inherently 5-D, extracting the reflectivity function using Fourier-based techniques directly would require complex and multi-dimensional calculations, including 4-D Fourier transforms (FTs) and interpolations to reduce the data to 3-D. To simplify this, the 5-D data  $H(x_i, x'_i, y_i, y'_i, f)$  is mapped to a 3-D dataset  $\tilde{H}(x''_i, y''_i, f)$ , where  $i'' = 1, 2, \dots, N_T N_R$ , and  $(x''_i, y''_i, 0)$  corresponds to the virtual elements displayed in the grid of Figure 1(b).

In an NF multistatic imaging scenario, aligning the raw data  $H(x_i, x'_i, y_i, y'_i, f)$  with the uniform grid in Figure 1(b) requires phase and amplitude compensations. Unlike in the FF scenario, where distances  $R_i$  and  $R'_i$  as well as their corresponding distance in the virtual grid (i.e.  $R''_i$  in Figure 2) are approximately equal and their differences negligible, this assumption is invalid in the NF scenario.

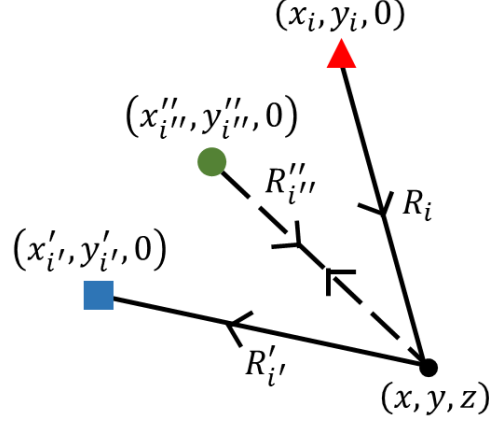


Figure 2. The locations and distances between the physical TX and RX antennas and the associated virtual element relative to a point scatterer.

By considering a scenario where the physical antennas at  $(x_i, y_i, 0)$  and  $(x'_i, y'_i, 0)$  have horizontal and vertical shifts  $\alpha_{i'}$  and  $\beta_{i'}$  relative to the virtual element coordinates  $(x''_i, y''_i, 0)$ , the distance  $R''_i$  can be computed by accounting for these shifts [13]. Equations (14) through (25) in [13] derive the total round-trip distance and an approximation using a 2-D Taylor series expansion.

Finally, approximations for the total round-trip distance and path loss in virtual elements are obtained, leading to the reduced-dimensionality data  $\tilde{H}(x''_i, y''_i, f)$  being expressed in the following simplified form [13]:

$$\tilde{H}(x''_i, y''_i, f) \approx \frac{z_0^2}{z_0^2 - (\alpha_{i'}^2 + \beta_{i'}^2)} \hat{H}(x_i, x'_i, y_i, y'_i, f) e^{jk \frac{\alpha_{i'}^2 + \beta_{i'}^2}{z_0}}, \quad (7)$$

where  $z_0$  represents the range in the center of the scene. By applying a 2-D FT to this data, the signal  $\tilde{\mathcal{H}}(k_x, k_y, k)$  in the wavenumber domain is derived, where the  $k_x$  and  $k_y$  axes of  $k$ -space correspond to the horizontal and vertical axes of the image [21]. Subsequent mathematical operations using the method of stationary phase [13, 22] yield the final signal expression in (8), which serves as a foundation for mapping the signal to a different domain (from  $\tilde{\mathcal{H}}(k_x, k_y, k)$  to  $\hat{\mathcal{H}}(k_x, k_y, k_z)$ ) using Stolt interpolation [13, 23]

$$\hat{\mathcal{H}}(k_x, k_y, k_z) = \frac{j}{8\pi\sqrt{k_x^2 + k_y^2 + k_z^2}} \int_V \frac{\rho(x, y, z)}{z} e^{-j(k_x x + k_y y + k_z z)} dV, \quad (8)$$

where

$$k_z = \sqrt{4k^2 - k_x^2 - k_y^2}, \quad 4k^2 - k_x^2 - k_y^2 \geq 0. \quad (9)$$

Finally, the reflectivity function is obtained as follows [13]

$$\rho(x, y, z) = -j8\pi z \text{FT}_{k_x, k_y, k_z}^{-1} \left\{ \sqrt{k_x^2 + k_y^2 + k_z^2} \hat{\mathcal{H}}(k_x, k_y, k_z) \right\}. \quad (10)$$

## 5. SIMULATION RESULTS AND DISCUSSION

In this section, the performance of the proposed method is examined using numerical simulations conducted in MATLAB. All simulations were carried out on MATLAB R2022b, running on a 64-bit Windows 11 system with 16 GB of random-access memory and a Core i7 central processing unit at 2.8 GHz. Unless stated otherwise, the simulation parameters are as detailed in Table 1, where  $\lambda$  denotes the wavelength corresponding to the highest frequency in free space and  $N_f$  is the number of uniformly distributed frequency samples.

Table 1. The values of the main simulation parameters.

Parameter	$N_x = N_y = N'_x = N'_y$	$d_x = d_y$	$d'_x = d'_y$	$L$	$f$	$z_0$	$N_f$
Value	11	$11\lambda/2$	$\lambda/2$	128	18-29 GHz	0.5 m	71

The first experiment compares the proposed approach with the conventional method (without signal coding, assuming temporal orthogonality) using the frequency response normalized mean square error (FRNMSE) criterion [13, 24] against code length and the number of TX antennas. The simulated channel amplitudes follow a Weibull distribution with shape and scale parameters of 1.8 and 0.975, respectively, ensuring  $\mathbb{E}\left\{\left|H_{i,i'}(f)\right|^2\right\}=1$  [13, 24]. The channel phases are uniformly distributed in the range  $[0, 2\pi)$ . Results are based on an average of 500 independent executions for different symbol-energy-to-noise-spectral-density ratios ( $E_s/N_0$ s) [25]. Figure 3(a) shows outputs for varying code lengths with  $N_T$  fixed at 3. The proposed method (solid lines) consistently outperforms the single TX case without coding (dashed lines), due to the added coding gain, which averages the noise power over  $L$  measurements. Mathematically, this means that the FRNMSE equals the estimated variance, i.e.  $\sigma_n^2/L$  [24], where  $\sigma_n^2$  is the measurement noise variance. As code length increases, the error decreases, consistent with the theoretical analysis [26] (as shown by the near-identical solid and dotted lines in Figure 3(a)). Next, the FRNMSE changes with varying  $N_T$  are examined with fixed code length. The results, shown in Figure 3(b), reveal that coded signals (solid lines) show lower errors, independent of the number of TX antennas. This is due to the mutual orthogonality of the codes from different TXs. In both Figures 3(a) and 3(b), it is quite expected that an increase in  $E_s/N_0$  leads to a decrease in FRNMSE.

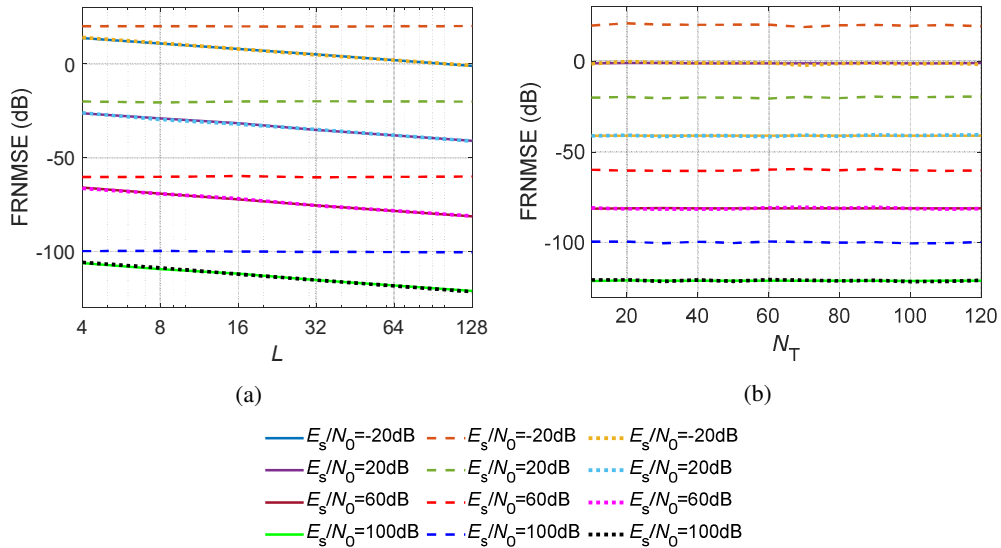


Figure 3. Comparison of FRNMSE values, (a) versus code length,  $N_T = 3$ , (b) versus the number of TXs. Dashed lines, solid lines and dotted lines are associated with the outputs without any coding, the outputs of the proposed approach and values of  $\sigma_n^2/L$ , respectively.

This experiment evaluates the impact of derived terms and approximations on the proposed algorithm's performance. Three point scatterers are positioned at  $(-0.05, -0.04, 1.01)$ ,  $(0, 0, 1.1)$  and  $(0.05, 0.04, 1.19)$  meters. Figure 4(a) presents the reconstructed image when amplitude terms are ignored, resulting in the farthest target being undetected due to propagation loss, a known issue with conventional range migration algorithm (RMA)-based techniques [13, 27]. Figure 4(b) shows the output with the amplitude terms included, effectively mitigating the propagation loss, now detecting all three targets.

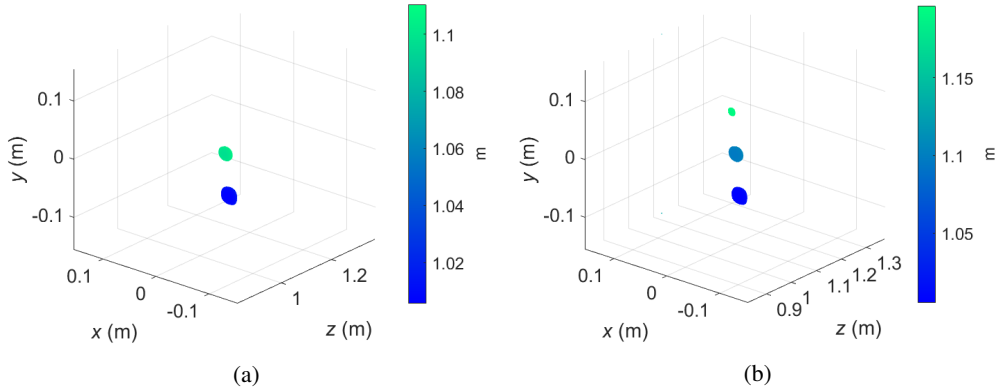


Figure 4. The isosurfaces of the images reconstructed by the proposed approach in 3-D view; (a) when the derived amplitude terms are ignored, (b) when the derived amplitude terms are fully included. The colorbar is range-coded, representing the distance.

In the final experiment, a T-shaped distributed target ( $0.099 \times 0.099 \times 0.01 \text{m}^3$ ) is used. The scene is defined by  $121 \times 121 \times 146$  voxels. Figure 5 shows the reconstructed images using the proposed approach. The output clearly identifies the target image. The proposed algorithm's total computational time, considering major operations like transfer function extraction, Fourier calculations, and Stolt interpolation, is 0.93 seconds. This is while the study [13] indicates that in the same scenario, with the same parameter values, the computing time for image reconstruction using the generalized synthetic aperture focusing technique [28] is more than 1000 seconds. Note that the proposed approach, due to reduced Stolt interpolation calculations (from 5D-to-3D interpolation to 3D-to-3D one), logically performs even better than conventional Fourier-based MIMO RMA in terms of computational load [13, 18].

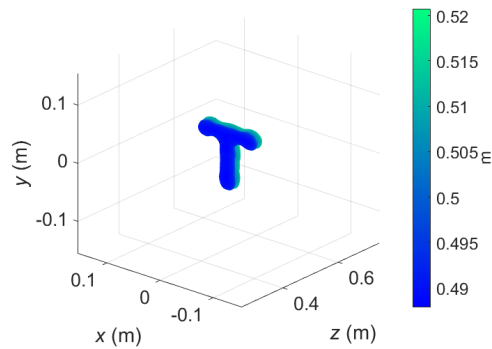


Figure 5. The isosurface of the reconstructed image of a T-shaped target by the proposed approach.

## 6. CONCLUSION

We presented an efficient approach to 3-D NF microwave imaging, integrating a 2-D MIMO configuration with orthogonal coding and a generalized reduced dimension Fourier algorithm. The proposed method successfully addresses the challenges associated with conventional imaging techniques, such as high computational complexity, large data acquisition requirements, and significant propagation loss in reconstructed images. By effectively reducing data dimensionality from 4-D to 2-D, the approach streamlines image reconstruction while preserving critical information.

Through mathematical derivations and simulations, we demonstrated that the proposed algorithm incorporates essential phase and amplitude compensations, crucial for accurate image reconstruction in NF scenarios. The inclusion of these compensators enables the algorithm to mitigate the effects of propagation loss, thereby improving the detection of distant targets. The numerical simulations validated the method's efficacy. The proposed algorithm reduces computational time significantly, making it a viable option for real-time applications.

## ACKNOWLEDGMENT

This work was funded by the Leverhulme Trust under the Research Leadership Award RL-2019-019.

## REFERENCES

- [1] C. Li and J. Lin, *Microwave noncontact motion sensing and analysis*. John Wiley & Sons, 2013.
- [2] R. K. Amineh, N. K. Nikolova, and M. Ravan, *Real-Time Three-Dimensional Imaging of Dielectric Bodies Using Microwave/Millimeter Wave Holography*. John Wiley & Sons, 2019.
- [3] A. M. Molaei *et al.*, "Application of Kirchhoff Migration Principle for Hardware-Efficient Near-Field Radar Imaging," *IEEE Transactions on Computational Imaging*, 2024.
- [4] O. Yurduseven, D. L. Marks, T. Fromenteze, J. N. Gollub, and D. R. Smith, "Millimeter-wave spotlight imager using dynamic holographic metasurface antennas," *Optics Express*, vol. 25, no. 15, pp. 18230-18249, 2017.
- [5] O. Yurduseven *et al.*, "Multibeam Si/GaAs holographic metasurface antenna at W-band," *IEEE Transactions on Antennas and Propagation*, vol. 69, no. 6, pp. 3523-3528, 2020.
- [6] K. B. Cooper *et al.*, "G-band radar for humidity and cloud remote sensing," *IEEE Transactions on Geoscience and Remote Sensing*, vol. 59, no. 2, pp. 1106-1117, 2020.
- [7] Y. Á. López, J. Laviada, A. Arboleya, and F. Las-Heras, "A Backpropagation Imaging Technique for Subsampled Synthetic Apertures," *IEEE Transactions on Instrumentation and Measurement*, vol. 72, pp. 1-16, 2023.
- [8] S. Hu, A. M. Molaei, and O. Yurduseven, "220 GHz sparse imaging with multi-static aperiodic array," in *Passive and Active Millimeter-Wave Imaging XXV*, 2022, vol. 12111: SPIE, pp. 83-89.
- [9] S. Hu *et al.*, "Multistatic MIMO sparse imaging based on FFT and low-rank matrix recovery techniques," *IEEE Transactions on Microwave Theory and Techniques*, vol. 71, no. 3, pp. 1285-1295, 2022.
- [10] T. Fromenteze, O. Yurduseven, F. Berland, C. Decroze, D. R. Smith, and A. G. Yarovoy, "A transverse spectrum deconvolution technique for MIMO short-range Fourier imaging," *IEEE Transactions on Geoscience and Remote Sensing*, vol. 57, no. 9, pp. 6311-6324, 2019.
- [11] A. M. Molaei, S. Hu, V. Skouroliakou, V. Fusco, X. Chen, and O. Yurduseven, "Fast processing approach for near-field terahertz imaging with linear sparse periodic array," *IEEE Sensors Journal*, vol. 22, no. 5, pp. 4410-4424, 2022.
- [12] M. Kuscü, E. Dinc, B. A. Bilgin, H. Ramezani, and O. B. Akan, "Transmitter and receiver architectures for molecular communications: A survey on physical design with modulation, coding, and detection techniques," *Proceedings of the IEEE*, vol. 107, no. 7, pp. 1302-1341, 2019.
- [13] A. M. Molaei, S. Hu, R. Kumar, and O. Yurduseven, "Mimo coded generalized reduced dimension fourier algorithm for 3-d microwave imaging," *IEEE Transactions on Geoscience and Remote Sensing*, vol. 61, pp. 1-15, 2023.
- [14] A. M. Molaei, S. Hu, V. Skouroliakou, V. Fusco, X. Chen, and O. Yurduseven, "Fourier compatible near-field multiple-input multiple-output terahertz imaging with sparse non-uniform apertures," *IEEE Access*, vol. 9, pp. 157278-157294, 2021.
- [15] K. J. Horadam, *Hadamard matrices and their applications*. Princeton university press, 2012.
- [16] K. Takei, "Balanced orthogonal code for polarization angle diversity," in *2014 Asia-Pacific Microwave Conference*, 2014: IEEE, pp. 938-940.
- [17] T. V. Hoang *et al.*, "Spatial diversity improvement in frequency-diverse computational imaging with a multi-port antenna," *Results in Physics*, vol. 22, p. 103906, 2021.
- [18] A. M. Molaei, T. Fromenteze, S. Hu, V. Fusco, and O. Yurduseven, "Fourier-based near-field three-dimensional image reconstruction in a multistatic imaging structure using dynamic metasurface antennas," *IEEE Transactions on Computational Imaging*, vol. 8, pp. 1089-1100, 2022.

- [19] O. Yurduseven, M. A. B. Abbasi, T. Fromenteze, and V. Fusco, "Frequency-diverse computational direction of arrival estimation technique," *Sci Rep*, vol. 9, no. 1, p. 16704, 2019.
- [20] O. Yurduseven, T. Fromenteze, C. Decroze, and V. F. Fusco, "Frequency-diverse computational automotive radar technique for debris detection," *IEEE Sensors Journal*, vol. 20, no. 22, pp. 13167-13177, 2020.
- [21] T. Küstner *et al.*, "LAPNet: Non-rigid registration derived in k-space for magnetic resonance imaging," *IEEE transactions on medical imaging*, vol. 40, no. 12, pp. 3686-3697, 2021.
- [22] L. Merabet, S. Robert, and C. Prada, "2-D and 3-D reconstruction algorithms in the Fourier domain for plane-wave imaging in nondestructive testing," *IEEE Transactions on Ultrasonics, Ferroelectrics, and Frequency Control*, vol. 66, no. 4, pp. 772-788, 2019.
- [23] A. Li, "Algorithms for the implementation of Stolt interpolation in SAR processing," in *IGARSS 1992; Proceedings of the 12th Annual International Geoscience and Remote Sensing Symposium*, 1992, vol. 1, pp. 360-362.
- [24] A. Pedross-Engel *et al.*, "Orthogonal coded active illumination for millimeter wave, massive-MIMO computational imaging with metasurface antennas," *IEEE Transactions on Computational Imaging*, vol. 4, no. 2, pp. 184-193, 2018.
- [25] V. Velez *et al.*, "System-level assessment of a C-RAN based on generalized space–frequency index modulation for 5G New radio and beyond," *Applied Sciences*, vol. 12, no. 3, p. 1592, 2022.
- [26] G. Yue, L. Ping, and X. Wang, "Generalized low-density parity-check codes based on Hadamard constraints," *IEEE Transactions on Information Theory*, vol. 53, no. 3, pp. 1058-1079, 2007.
- [27] A. M. Molaei *et al.*, "Development of fast Fourier-compatible image reconstruction for 3D near-field bistatic microwave imaging with dynamic metasurface antennas," *IEEE Transactions on Vehicular Technology*, vol. 71, no. 12, pp. 13077-13090, 2022.
- [28] D. M. Sheen, R. T. Clark, J. R. Tedeschi, A. M. Jones, and T. E. Hall, "Imaging systems and related methods including radar imaging with moving arrays or moving targets," ed: Google Patents, 2024.